Photovoltaic Devices: Opto-Electro-Thermal Physics and Modeling

*Aixue Shang and Xiaofeng Li**

Nano-/micro-structured thin-film solar cells (SCs) under advanced light management designs have attracted intensive attention due to their potential in realizing cost-effective solar energy utilization.[1] In these devices, thermal effects such as self-heating and light-induced heating are evident; this can heat up the device and constrain the output performance dramatically.[2] Especially, for concentrating photovoltaics, temperature rise under a high concentration ratio (e.g., 1000 suns) will bring a serious challenge to sustain the operation stability of SCs. Hence, the thermal effects play important roles in determining the SC performance. The consideration of this important mechanism not only enables a thorough understanding of the multi-domain photovoltaic physics but also leads to many new application possibilities. For example, passive radiative cooling presented by Fan's group has been considered promising for cooling down SCs for higher photoconversion efficiency.[3] Therefore, it is obvious that the photovoltaic devices are not just the optical and electrical systems, but also typical thermodynamic systems; these three physical domains are tightly coupled.

Previous simulations for SCs mainly focus on the optoelectronic analysis with addressing electromagnetic and electrical responses,[4] which not only maximize light absorption but also ensure that the generated carriers can be efficiently collected. For example, coupled optical and electrical modeling of nanostructured SCs was reported to simultaneously increase the light absorption and optimize the electrical properties of α-Si:H cell.[5] A thorough optoelectronic simulation has been conducted for nanowire and nanohole SCs, revealing that nanowire and nanohole SCs have a superior light harvesting capability than planar devices and that radially doped SCs are more efficient for carrier collection than axially doped systems.[4d] However, previous optoelectronic studies are performed with the assumption that SCs are operating under standard test condition (STC),[6] where the air mass index is 1.5, the solar irradiance P_s = 1000 W m^{-2}, and the ambient temperature T_{amb} = 25 ± 1 °C. Moreover, the operating temperature of SCs (i.e., T) is set to be equal to T_{amb} by default. In reality, the temperature of SCs will increase sharply due to thermal effects and in turn affect the output performance.[7] A thorough treatment on the optoelectronic and thermodynamical response in spatial and frequency domains is strongly desired in order to promote the understanding of SCs as well as explore novel photovoltaic designs for high efficiency and high stability.

In this study, taking a single-junction gallium arsenide (GaAs) SC as an example, we present our progress on photovoltaic simulation with considering the optoelectronic and thermodynamic mechanisms simultaneously. We use finite-element method (FEM) under the platform of COMSOL Multiphysics to investigate the electromagnetic absorption, nonisothermal carrier transport, and heat flow inside the SCs.[8] Optically, we investigate light absorption, reflection, and transmission by solving the Maxwell's equations. Electrically, various carrier loss mechanisms arising from surface and bulk recombinations, carrier drift driven by electric field, and carrier diffusion caused by the gradient of carrier concentration and lattice temperature are extensively treated.[6,9] Owing to phonon scattering and carrier recombination, a fraction of energy is not electrically usable and converted to heat ultimately. Thermodynamically, heat generation (due to thermalization, Joule heat, Peltier heat, and recombination heat) and heat dissipation (such as convective and radiative cooling) are taken into consideration.[10] Benefited from such an opto-electro-thermal (OET) simulation technique, energy conversion from light incidence to electricity and thermal energy is quantified under various biases, enabling a deep insight into the intrinsic OET fundamentals of SCs. Considering that the light-trapping strategies for SCs have been extensively reported,[11] here we preferentially concentrate on the OET physics and simulation technology of SCs rather than the specific designs for high performance. Therefore, although only a single-junction GaAs SC is presented, this methodology is applicable for a broad range of photoconversion devices (including SCs and photodetectors) composed by various material systems under specific configurations. This study is beneficial to accurately predict the performance and guide the design of advanced photovoltaic devices.

Based on our previous optoelectronic model,[4] OET simulation can be realized with including the thermodynamic module. Here, we use a rigorous thermodynamic treatment of heat generation and conduction according to the literatures by Wachutka;[12] moreover, a single-junction GaAs SC (Palik's data for GaAs material[4a]) with a thickness of 1 µm equipped with dual-layer antireflection coatings (ARC) of ZnS and MgF_2 is employed as the platform for the OET study.[4a,9a] The discussions are based on the following assumptions: (1) hot-carrier

Dr. A. Shang, Prof. X. Li
College of Physics, Optoelectronics and Energy
and Collaborative Innovation
Center of Suzhou Nano Science and Technology
Soochow University
Suzhou 215006, China
E-mail: xfli@suda.edu.cn
Dr. A. Shang, Prof. X. Li
Key Lab of Advanced Optical Manufacturing Technologies of Jiangsu
Province and Key Lab of Modern Optical Technologies of Education
Ministry of China
Soochow University
Suzhou 215006, China

DOI: 10.1002/adma.201603492

© 2016 WILEY-VCH Verlag GmbH & Co. KGaA, Weinheim

effects are omitted and it finally arrives at the postulation that both electrons and holes are in thermal equilibrium with the lattice; (2) photon recycling is taken into account by using a reduced radiative coefficient according to the data from ref. [4a]; and (3) solar irradiance with $P_s = 1000$ W m^{-2} (i.e., the standard AM1.5 solar spectrum is used as the source of this simulation) and the ambient temperature (T_{amb} = 25 °C) is different from the lattice temperature T. The coupled equations governing the OET responses of SCs are[4,12]

$$\nabla \times (\nabla \times E) = k_0^2 \varepsilon_r E \tag{1}$$

$$G(x,y,z) = \int g(x,y,z,\lambda) \mathrm{d}\lambda \tag{2}$$

$$\nabla \cdot \left[-D_n \nabla n + n\mu_n \left(\nabla \Phi + \frac{\nabla \chi}{q} + \frac{K_B T}{q} \nabla \ln N_c \right) - n D_{th}^n \nabla T \right] = G(x,y,z) - U \tag{3}$$

$$\nabla \cdot \left[-D_p \nabla p - p\mu_p \left(\nabla \Phi + \frac{\nabla \chi}{q} + \frac{\nabla E_g}{q} - \frac{K_B T}{q} \nabla \ln N_V \right) - p D_{th}^p \nabla T \right] = G(x,y,z) - U \tag{4}$$

$$\nabla^2 \Phi = \frac{q}{\varepsilon_0 \varepsilon_r} (n - p - C) \tag{5}$$

$$\nabla \cdot (-k \nabla T) = H \tag{6}$$

where k_0 is wave vector in free space, ε_r the material permittivity, n (p) the electron (hole) concentration, Φ the electrostatic potential, D_n (D_p) the electron (hole) diffusion coefficient, D_{th}^n (D_{th}^p) the thermal diffusion coefficient for electron (hole), N_c (N_v) the effective conduction (valence) band density of states, μ_n (μ_p) the electron (hole) mobility, K_B the Boltzmann's constant, U the total bulk recombination, q the electron charge, C the impurity concentration, k the total thermal conductivity, and H the total heat generation to be specified in the following. The values of the parameters such as mobilities and carrier lifetimes can refer to our previous works.[4]

We first solve the electromagnetic wave equation in frequency domain under a normal incidence, so that the absorption response and the wavelength-dependent carrier generation rate $g(x, y, z, \lambda)$ of the SCs can be accessed. For this planar system under normal incidence, the system responses under transverse electric (TE) and transverse magnetic (TM) incidences are identical; however, if the rotationally asymmetrical components are involved or under an oblique incidence, TE and TM incidences have to be considered separately (the unpolarized incidence takes the average of TE and TM cases).[4] The total generation rate [i.e., $G(x, y, z)$] can be expressed as the spectral integral of $g(x, y, z, \lambda)$ over the whole material absorption band as indicated in Equation (2).[13] Carrier transport and Poisson's equation are expressed in Equations (3)–(5), where carrier drift and diffusion have been considered. It should be mentioned that the gradient of lattice temperature acts as an additional force to drive the carriers;[14] therefore, the carrier transport equations become strongly temperature-dependent and heat generation is actually closely related to carrier motion and light absorption.

Let us have a brief view of the microscopic processes in photovoltaic systems shown in **Figure 1**, where the incident photons deliver energy to carriers and lattice, generating photocurrent and heat. The schematic diagram depicts energy band of typical homojunction SCs operating under a forward electrical bias V_a. The main thermodynamic processes are as follows.[12,15]

(a) *Thermalization*. For the incident photons with energy $h\nu > E_g$, they can be absorbed by the material to generate electron–hole pairs with high kinetic energy. Through the scattering at the crystal lattice, electrons (holes) will thermalize to the conduction (valence) band edge in picoseconds. The energy released in this process can be expressed as

$$H_{th}(x,y,z) = \int (h\nu - E_g - 3K_B T) \cdot g(x,y,z,\lambda) \mathrm{d}\lambda \tag{7}$$

where $h\nu - E_g - 3K_B T$ is the excess energy of a photon incidence (unit: eV) with a specific wavelength and $g(x, y, z, \lambda)$ (unit: photons m^{-3} s^{-1} nm^{-1}) is the corresponding carrier generation rate. $3K_B T$ denotes thermal average values from electrons and holes as indicated in ref. [12a].

(b) *Joule heat*. The motion of photogenerated carriers will generate photocurrent as well as Joule heat due to the acceleration of carriers in the electric field. This process mainly happens in the depletion region where the electric field is strong. Joule heat is normally regarded as the main self-heating mechanism in semiconductor devices and can be described as[12a,14]

$$H_{Joule}(x,y,z) = F \cdot J \tag{8}$$

where J is the total photocurrent from electrons and holes, and F is the electric field defined as the negative gradient of the electrostatic potential, i.e., $F = -\nabla \Phi$.

(c) *Bulk recombination*. We consider three typical bulk recombinations including radiative, Shockley–Read–Hall (SRH), and Auger contributions. The last two can also be classified as the non-radiative recombination. Energy flow between carriers and lattice is enabled by SRH recombination and energy exchange between carriers is realized by Auger recombination, which will heat up the SCs ultimately when reaching the thermodynamic equilibrium. Nevertheless, the energy exchange between carriers and ambient through radiative recombination makes no contribution to the thermodynamic system of SCs. Auger recombination coefficient is 1×10^{-30} cm^6 s^{-1} for both electrons and holes. Considering photon recycling, a properly reduced radiative recombination coefficient $\approx 1.5 \times 10^{-10}$ cm^3 s^{-1} is used.[4a] Heat generation due to non-radiative recombination is expressed as[12]

$$H_{non\text{-}rad}(x,y,z) = (E_g + 3K_B T) \cdot (U_{SRH} + U_{Aug}) \tag{9}$$

© 2016 WILEY-VCH Verlag GmbH & Co. KGaA, Weinheim

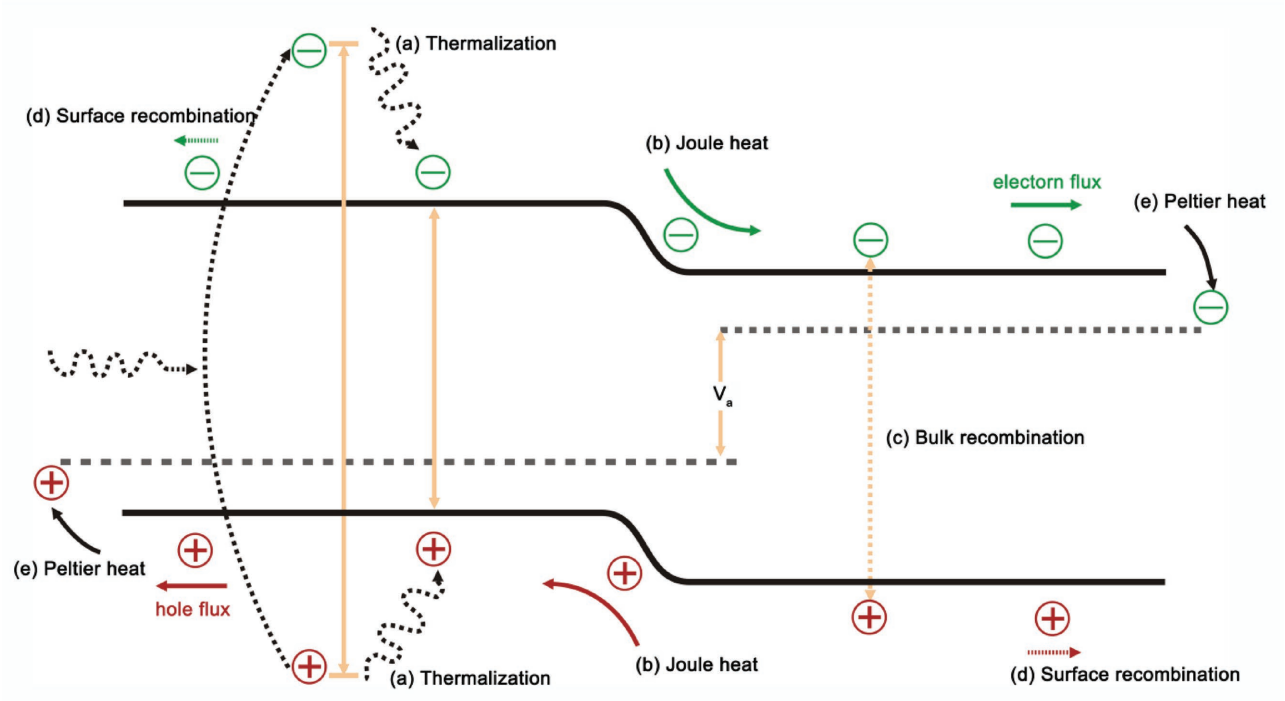

Figure 1. Loss process in a single-junction GaAs solar cell: a) thermalization, b) Joule heat, c) bulk recombination, d) surface recombination, and e) Peltier heat.

where U_{SRH} (U_{Aug}) denotes SRH (Auger) recombination rate. The total non-radiative recombination rate $U_{non\text{-}rad} = U_{SRH} + U_{Aug}$.

(d) *Surface recombination*. When minorities reach the cell surface with lattice defects, they will be depleted via the surface recombination and release the energy to heat up the SCs. The released heat can be calculated by

$$H_{surf} = \left(E_g + 3K_B T\right) \cdot U_{surf} \tag{10}$$

where U_{surf} is the surface recombination rate.[4d]

(e) *Peltier heat*. Before being collected by the external circuit, electrons (holes) have to flow from conduction (valence) band to the corresponding quasi-Fermi level and release energy to the lattice, namely, the Peltier effect. The value of Peltier heat for electron (hole) is related to the energy difference of conduction (valence) band and the corresponding quasi-Fermi levels as shown as[16]

$$H^{n}_{Peltier} = \left(E_c + 1.5K_B T - E_{fn}\right) \cdot J \tag{11}$$

$$H^{p}_{Peltier} = \left(E_{fp} - E_v + 1.5K_B T\right) \cdot J \tag{12}$$

where E_c (E_v) is the conduction (valence) level and E_{fn} (E_{fp}) the electron (hole) quasi-Fermi level.

In the above equations, H_{th}, H_{Joule}, and $H_{non\text{-}rad}$ are the volume thermal density with unit W m^{-3}, while H_{surf}, $H^{n}_{Peltier}$ and $H^{p}_{Peltier}$ take place on the surfaces as boundary conditions with unit W m^{-2}. Besides, the heat generation rate (H_{ARC}) in ARC layers is identical to the energy of absorbed photons by these layers.

To finalize the model introduction, we would like to summarize the boundary conditions in optical, electrical, and thermal modules for the OET simulation. In the transverse direction (vertical to the semiconductor junction), period boundaries are used for all modules. However, for the boundaries along the junction, the conditions are quite distinguished. Specifically, (1) for the optical module, perfectly matched layers (PMLs) are used on the top and bottom sides of the cell to avoid the unphysical reflection; (2) for the electrical module, surface recombinations are used to define the top and bottom boundaries;[4a] (3) for the thermodynamic module, the top and bottom boundaries are composed of several heat components, that is, the convection heat, surface radiation heat, Peltier heat, and surface recombination heat.[4d,9a,12]

Having categorized the heat-induced energy losses and uncovered the microscopic processes arising from various semiconductor mechanisms in photovoltaic systems (see Figure 1), we can now turn our attention to examine how the incident energy is consumed by all these effects. Obtaining this profound information is critical for better understanding and controlling the operations of photovoltaic devices. Based on our OET simulation, **Figure 2** illustrates how the total solar irradiance (P_s = 1000 W m^{-2}) is decomposed into various parts in the investigated SC under the optimal voltage (i.e., corresponding to the maximized output power). Here, single-junction GaAs SC with ARC layers is considered, where the incident photons deliver energy to the cell, generate photocurrent to drive external circuit, and produce excess energy to heat up the

© 2016 WILEY-VCH Verlag GmbH & Co. KGaA, Weinheim

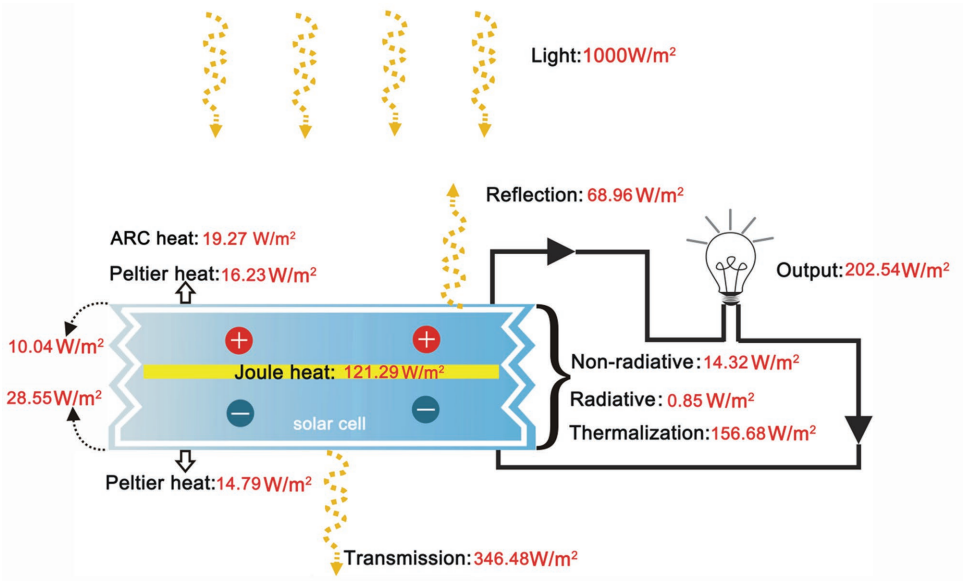

Figure 2. A sketch of photovoltaic system is vividly plotted where the distribution of power densities is quantified under optimal forward bias.

device. First, the total power of incident photons is 1000 W m^{-2} and the power losses from the optical reflection and transmission are 68.96 and 346.48 W m^{-2}, respectively, leaving the rest (i.e., 584.56 W m^{-2}) to be absorbed by the SC. It is obvious that: (1) the reflection loss is low, attributed to the good optical performance of dual-layer ARC design; (2) since the thickness of the photoactive layer is very thin (only 1 µm), the light transmission (including the unabsorbed over-bandgap incidence and the below-bandgap energy) is evident and leads to a large energy loss (to capture photons more efficiently, light management strategies based on nanostructure designs have to be used[11]). Second, only 202.54 in 584.56 W m^{-2} is available for the electricity output, revealing that a large portion of energy has been wasted. For example, a small fraction of energy loss due to radiative recombination is 0.85 W m^{-2}, which goes back to the ambient in the form of photons without heating up the SC; the rest energy loss is as high as 381.17 W m^{-2}, which is converted into heat via various ways. Among them, thermalization is the dominant factor, spending a high energy of 156.68 W m^{-2} to elevate the cell temperature via phonons. Energy loss due to Joule heat is also significant, that is, 121.29 W m^{-2}, which is also a very important ingredient in regulating the operation of many thermodynamic systems (e.g., it is regarded as the key factor of self-heating in semiconductor devices[15a]). Joule heat is determined by the material itself such as mobility and carrier density and is thus hard to be removed. The rest energy losses are relatively low, but still influence the device operation status to some degree as discussed below. (1) Non-radiative recombination leads 14.32 W m^{-2} of the energy to be converted into heat due to the carrier–lattice interaction. Apparently, this part of energy can be reduced under a low non-radiative recombination rate as indicated in Equation (9). Therefore, the purity of material and low trap density are essential for high-efficiency photovoltaic systems. (2) Surface recombination also makes a waste of energy to heat. In top (bottom) surface of the considered GaAs cell, the energy loss is 10.04 W m^{-2} (28.55 W m^{-2}), which is determined by the surface recombination rate [see Equation (10)]. Surface recombination can be suppressed by using passivation technology and window or BSF (back surface field) layer. (3) Heat generation arising from Peltier heat in p-contact (n-contact) is 16.23 W m^{-2} (14.79 W m^{-2}) in this study. (4) As the ARC is not entirely transparent, it leads to an energy loss of 19.27 W m^{-2} noted as the ARC heat in the sketch.

Figure 2 solely displays the situation under the optimal electrical bias; nevertheless, the photocurrent and power density of SCs exhibit quite unique behaviors which are strongly dependent upon the operation situation (e.g., the forward electrical bias V_a). For the convenience of comparison, we evaluate the effects of all mechanisms by equivalently calculating the corresponding photocurrent. That is, for cell output, it is the photocurrent available for the external load; while for surface and bulk recombinations, they are the photocurrents which have been wasted without exporting electricity. Plotted in **Figure 3** are the photocurrent densities versus the forward electrical bias caused by various internal semiconductor mechanisms. It should be noted that J_{ph} is the photogenerated current density, which is directly converted from photon absorption without addressing any electrical losses (i.e., internal-quantum efficiency, IQE, is 100%); therefore, J_{ph} (= 271.20 A m^{-2}) is independent of V_a and represents the upper limit of the photocurrent. J_{ph} can be divided into the following several parts. A large portion is the output photocurrent J. From J–V_a curve we can get the short-circuit photocurrent density J_{sc} = 248.36 A m^{-2}, the open-circuit voltage V_{oc} = 0.96 V, and the optimal voltage of 0.86 V. It is obvious that J is decreasing slowly when V_a is low (e.g., V_a < 0.6 V) and drops fast when V_a is high (e.g., V_a > 0.8 V) due to the dramatically increased dark current. For a further insight into the dark current, we distinguish the various contributions of dark current by examining the photocurrent losses arising from the surface (top and bottom surfaces, J^{T}_{surf} and J^{B}_{surf}) and bulk recombinations (J_{bulk}) in Figure 3. It is found that all these carrier recombinations do not change apparently

© 2016 WILEY-VCH Verlag GmbH & Co. KGaA, Weinheim

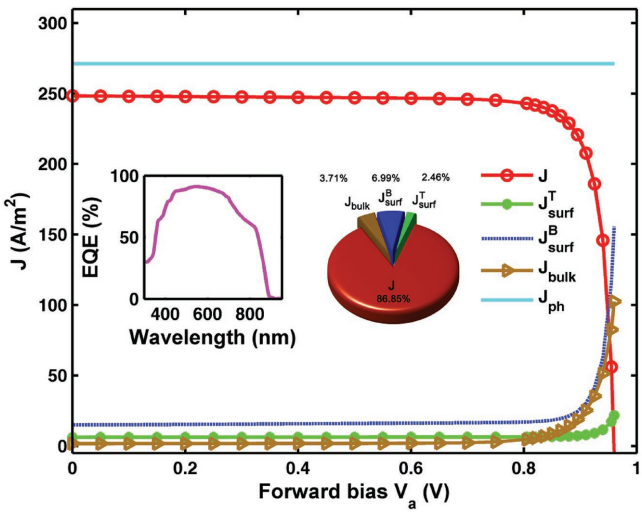

Figure 3. Quantified photocurrent losses arising from the bulk and surface carrier recombinations under various biases are investigated. The left inset is the EQE spectrum under the short-circuit condition; the right inset is the pie chart of the photocurrent distribution.

with increasing V_a when V_a is small. Keeping increasing V_a to be close to V_{oc}, carrier recombinations (especially, the bottom surface recombination and the bulk recombination) are sharply strengthened. Comparing J^B_{surf} and J^T_{surf}, the former is much higher, showing that the surface recombination on the bottom surface dominates the whole surface recombination effect. This is because in the considered GaAs SC the depletion region is much closer to the top surface and thus the carrier separation is more effective in the top region, preventing the minorities from reaching the top surface for recombination. For a further insight into the microscopic response of the SC, we plot the spectrum of external quantum efficiency (EQE) in this figure. EQE is low at short-wavelength region due to the surface recombination and reduces to zero at below-bandgap band. Besides, we also draw a pie chart in Figure 3 for the situation with the optimal forward bias ($V_a = 0.86$ V). We can see that: (1) the output photocurrent density J accounts for 86.85% of the whole photogenerated current; (2) J^B_{surf} is dominant mechanism of the photocurrent loss and leads 6.99% of J_{ph} to be wasted; (3) J_{bulk} accounts for 3.71% in this device with a thin photoactive layer; (4) 2.46% of the photocurrent is wasted due to the top surface recombination. Although J_{ph} is from the electromagnetic calculation and the rest current components from our OET simulation, we find that these calculations exhibit a perfect conservation as the following

$$J_{ph} = J + J_{bulk} + J^T_{surf} + J^B_{surf} \tag{13}$$

Above equation verifies that our OET simulation is accurate enough. Such a current conservation can also be derived directly from the continuity Equations (3) and (4), with considering the boundary conditions for minority surface recombination.[4d,9a] In the following discussion on the power density, similar conservation will also be achieved successfully.

Here, we would like to indicate that the discrimination on the various photocurrent gain/loss components in Figure 3 is only for the energy which has been successfully absorbed by the SC. A more complete picture should be based on the overall energy from the solar incidence so that one can get the detailed destinations of the energies driven by various microscopic semiconductor mechanisms. Therefore, in the forthcoming discussion, we unite the unit of W m^{-2} to describe all energy portions. This can be implemented by integrating the volume (areal) heat power densities [see Equations (7)–(12)] in the whole device (surface) and then dividing the integrated heat powers by the area of the device surface. The bias-dependent power densities for all considered semiconductor mechanisms are plotted in **Figure 4**a,b, respectively. Figure 4 is actually an extended version of the diagram shown in Figure 2 by including the dependence on the electrical bias.

As mentioned previously, excluding the optical reflection and transmission, the total power density (P_{ph}) of the absorbed photons is 584.56 W m^{-2}, which is independent of the forward bias, that is, a straight line in Figure 4. Only a fraction of P_{ph} is available for the electrical output and the rest is converted into heat or wasted through radiative recombination (excluding the reabsorption due to the photon recycling). The maximum output power density ($P = 202.54$ W m^{-2}) is achieved when $V_a = 0.86$ V, as also indicated in Figure 2. P_{Joule} denotes the power loss due to the Joule effect. Interestingly, when $V_a = 0$ V, P_{Joule} is maximized because at the condition the built-in electric field is the highest (compared to the forward electrical bias) to exert the strongest force to push the electrons and holes inside the semiconductor junction. When $V_a = V_{oc}$, the electric field is evidently weakened and $J = 0$ A m^{-2} so that $P_{Joule} = 0$ W m^{-2} [see Equation (8)]. Power loss arising from the thermalization process (P_{th}) is plotted in Figure 4a by the dotted line, which seems to be straight but is still dependent on the operating temperature T [see Equation (7)]. We can find that P_{th} and P_{Joule} are the key ingredients for thermal energy. Besides, P_{ARC} is the power loss in antireflection coatings converted directly from the light absorption. P_{ARC} is independent of V_a and as low as 19.27 W m^{-2} as also indicated in Figure 2. Other power losses due to Peltier effect and carrier recombination are plotted in Figure 4b. $P_{Peltier}$ refers to the power loss caused by Peltier effect, which is essentially constant under a low forward bias ($V_a < 0.6$ V) while diminishes sharply under a high V_a with $P_{Peltier} = 0$ W m^{-2} when $V_a = V_{oc}$. Top and bottom surface recombinations make up a power loss of P_{surf}, which is similar to the curve of $P_{Peltier}$ under a low V_a. However, P_{surf} elevates rapidly when $V_a > 0.8$ V and then becomes the leading power loss. P_{rad} is not very large in all investigated forward biases so that only a small fraction of energy is released to the ambient via radiative recombination. Comparably, $P_{non\text{-}rad}$ is much more important and shows as well a rapid increment with increasing V_a toward V_{oc}. In these power losses, P_{Joule}, P_{th}, P_{ARC}, $P_{Peltier}$, P_{surf}, and $P_{non\text{-}rad}$ will heat up the SC so that we can have the expression

$$\frac{1}{A}\int \nabla\cdot(-k\nabla T)\,\mathrm{d}\Omega = P_{Joule} + P_{th} + P_{ARC} + P_{Peltier} + P_{surf} + P_{non\text{-}rad} \tag{14}$$

where the left term is the total heat generation term in Equation (6) and Ω (A) is the spatial domain (area of contact

© 2016 WILEY-VCH Verlag GmbH & Co. KGaA, Weinheim

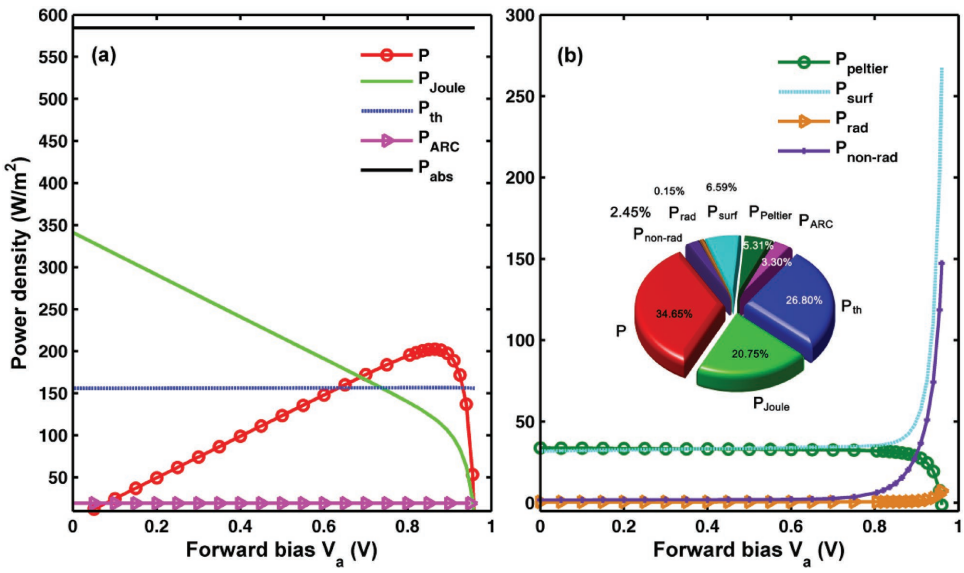

Figure 4. Quantified power densities arising from various mechanisms are investigated. a) Power density curves such as output power, Joule heating power, thermalization power, ARC power, and total photo-generated power. b) The power densities loss due to Peltier effects and recombinations. The inset in (b) shows the percentage of each power loss in the total power density when the solar cell operates under optimal voltage.

surface). Owing to the energy conservation, we finally arrive at another conservation expression

$$P_{\mathrm{ph}} = P + P_{\mathrm{rad}} + \frac{1}{A}\int \nabla\cdot(-k\nabla T)\,\mathrm{d}\Omega \tag{15}$$

where the incoming energy fluxes (i.e., P_{ph} = 584.56 W m^{-2}) in the above equation can be divided into three parts. P is electrically usable and determines the output performance of the SC and P_{rad} refers to the energy loss due to photon emission under radiative recombination. The last part is related to heat generation contributed by various heat sources [see Equation (14)].

Heat generation is discussed based on rigorous treatment above, which will heat up the SCs and increase the operating temperature. However, the operating temperature should reach a stable level owing to heat dissipation such as convective cooling and radiative cooling, which are also considered in this OET simulation. **Figure 5**a shows the calculated convective cooling ($H_{\mathrm{con}}^{\mathrm{cool}}$) and radiative cooling ($H_{\mathrm{rad}}^{\mathrm{cool}}$) as a function of the forward bias. $H_{\mathrm{con}}^{\mathrm{cool}}$ is determined by

$$H_{\mathrm{con}}^{\mathrm{cool}} = h(T - T_{\mathrm{amb}}) \tag{16}$$

where h is the convective coefficient and T (T_{amb}) the device (ambient) temperature. In this calculation, h = 6 W m^{-2} K^{-1} is much easily affected by wind speeds.[3b] $H_{\mathrm{rad}}^{\mathrm{cool}}$ denotes the power loss due to surface radiative cooling and obeys the formula

$$H_{\mathrm{rad}}^{\mathrm{cool}} = \varepsilon\sigma\left(T^4 - T_{\mathrm{amb}}^4\right) \tag{17}$$

where ε = 0.8 is surface emissivity in the calculation and σ is Stefan–Boltzmann constant. There is no doubt that we can reach a thermal balance law

$$\frac{1}{A}\int \nabla\cdot(-k\nabla T)\,\mathrm{d}\Omega = \frac{1}{A}\int\left(H_{\mathrm{con}}^{\mathrm{cool}} + H_{\mathrm{rad}}^{\mathrm{cool}}\right)\mathrm{d}A \tag{18}$$

From Figure 5a, we can find that $H_{\mathrm{con}}^{\mathrm{cool}}$ and $H_{\mathrm{rad}}^{\mathrm{cool}}$ show similar trends with varying V_{a}. Cooling effect reaches the lowest when the SC is operating at the optimal voltage. This is reasonable since at this condition the output power reaches the maximum, leaving only a fraction of energy to be converted into heat. When the SC is operating at J_{sc} or V_{oc} condition, cooling effect is quite evident because there is no power output and almost all of the absorbed energy is converted into heat. In addition, convective cooling is about 2.2 times over surface radiative cooling, as indicated in ref. [17].

After finishing the analysis of photocurrent, heat generation, and dissipation in SCs, we finally discuss the stabilized operating temperature. As we can observe in the equations above, many of them are strongly related to T. Therefore, the device temperature plays an important role in determining the OET performance of SCs. In this study, the thermal conductivities of MgF_2, ZnS, and GaAs are 21, 14, and 33 W m^{-1} K^{-1}, respectively. By solving the coupled Equations (3)–(6) and taking account of the heat generation and dissipation, we can obtain the distribution of temperature (i.e., T) in the cell. Since the investigated SC is very thin, T variation in space is quite small. However, if we consider more complicated configurations (e.g., plasmonic SCs), strongly space-dependent T can be observed. The T variation with V_{a} is shown in Figure 5b. Being similar to the curves in Figure 5a, T is minimized under the optimal voltage while increases sharply up to 56.7 °C at $V_{\mathrm{a}} = V_{\mathrm{oc}}$, which is consistent with an empirical formula rewritten below[18]

$$T = 0.943\times T_{\mathrm{amb}}(^{\circ}\mathrm{C}) + 0.028\times \mathrm{Irradiance} - 1.528\times \mathrm{WindSpd} + 4.3 \tag{19}$$

© 2016 WILEY-VCH Verlag GmbH & Co. KGaA, Weinheim

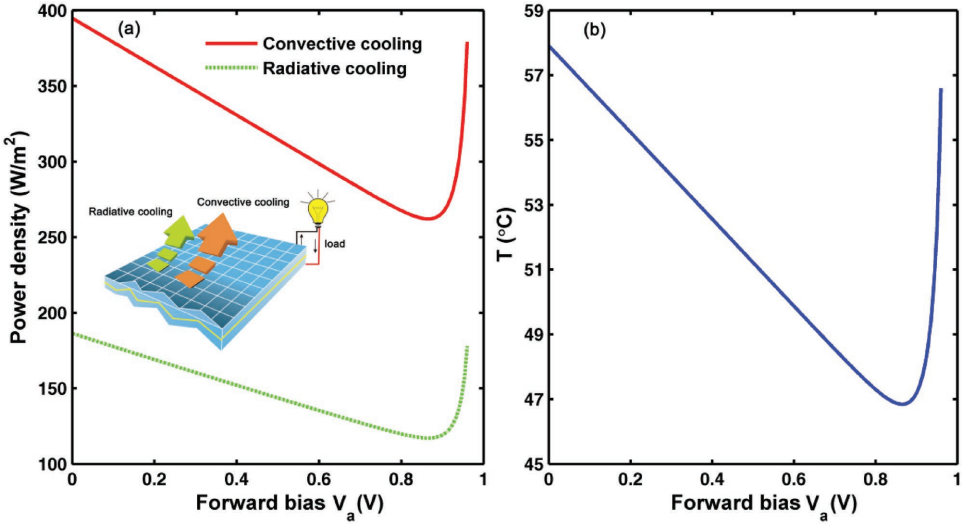

Figure 5. a) Convective cooling and radiative cooling are investigated and b) operating temperature of solar cell under various biases is plotted.

where Irradiance (WindSpd) refers to solar irradiance (wind speed) with unit W m^{-2} (m s^{-1}). Using the empirical formula and setting T_{amb} = 25 °C, solar irradiance of 1000 W m^{-2}, and wind speed of 1 m s^{-1}, we can get T = 54.3 °C, which agrees well with our simulation. A small discrepancy is from the difference in the SC configuration.

The analysis of SCs from the viewpoint of energy is the most fundamental understanding of photovoltaic principles. We often concentrate on output power of a SC and find solutions to promote the light-conversion efficiency. However, a comprehensive recognition of power density loss provides a convenient hint to improve the cell efficiency. Let us have a brief review on the basic strategies to improve the photovoltaic efficiency. For the conventional optical consideration, light trappings such as utilizing antireflection coatings, photonic crystal, or plasmonics are proved to be effective for the performance promotion, which can be classified as photon management.[19] From the perspective of photocurrent, carrier recombination can be reduced by good surface passivation and purifying the material to be with low trapping densities, which can be regarded as the carrier management.[19] However, it is not enough since there are more ways to further improve the cell performance. Considering the vast over-bandgap energy loss, we can use multi-junction or hot-carrier technologies to make full use of the excess energy. In this study, we also mentioned that Joule heating and Peltier heating are related to the doping profiles and carrier mobility so that they can be controlled and reduced by properly optimizing the doping profile. However, if we change the doping profile, the electrical behaviors, for example, carrier transportation and recombination, will also be modified, which brings us new challenge for a comprehensive design. To date, there are rare reports on manipulating the Joule heating and Peltier heating in SCs. We consider this as the heat management, which deserves a thorough investigation in the future. By using the proposed OET simulation method, the mentioned optical, electrical, and thermodynamic behaviors can all be studied in a comprehensive way, providing us a new opportunity to better understand photovoltaic devices for novel designs.

In conclusion, we reported a full-coupled optoelectronic and thermodynamic simulation for photovoltaic cells, where fundamental physics are thoroughly discussed by addressing optical, electrical, and thermal effects simultaneously. First, we introduced a schematic diagram of energy level to reveal the intrinsic microscopic processes of SCs, where photons, carriers, and lattice make up the complicated system and the interactions between them were discussed in detail. We then illustrated the quantified energy distributions in the photovoltaic system under the operation voltage so that one can get a further insight into the energy conversion and exchange in SCs. We further investigated quantitatively the various photocurrents (e.g., J, J_{bulk}, J^{T}_{surf}) and power energies (e.g., P, P_{Joule}, $P_{Peltier}$) with varying the forward electrical bias, which enable delicately distinguishing the various photocurrent (energy) gained or consumed due to various OET mechanisms. Moreover, the energy conservation was achieved for both photocurrent and power density analyses. Finally, we estimated the heat dissipation with considering the convective cooling and surface radiative cooling and predicted the stabilized operation temperature of the SC. It is found that the lowest temperature rise can be achieved when the cell is working with the highest output.

The proposed OET simulation technique provides a readily way to look deep inside into the fundamental physics and light–matter interactions in photovoltaic devices, which is beneficial for fundamental studies as well as advanced device developments. We would also like to indicate that SCs based on various photoactive materials show distinguished optical, electrical, and thermal effects due to unique absorbing band, absorption coefficient, electron/hole diffusivity, electron/hole lifetime, etc. However, for each kind of SC, the basic operation and intrinsic OET mechanisms are unchanged. Therefore, most of the conclusions in this paper are qualitatively applicable for other devices, although the quantities (response details) will be varied depending on the materials and the system structures. Moreover, this methodology can find a broad range of applications for the design of optoelectronic devices. For instance, (1) photodetectors are working with a similar principle and can

© 2016 WILEY-VCH Verlag GmbH & Co. KGaA, Weinheim

be simulated with addressing the OET and photoresponsivity characteristics; (2) the plasmonic devices show quite unique thermal effect under the strong field-localization effect and can be studied as well; (3) especially, for the multi-junction SCs with a high solar concentration, thermal response is critically important, which has to be taken into account in the device design; (4) more novel photovoltaic devices can be developed by addressing the OET response, including the previously mentioned SCs configured with self-cooling photonic crystal nanostructures.[3]

Acknowledgements

This work was supported by National Natural Science Foundation of China (Nos. 61675142 and 91233119), the Youth 973 Program (No. 2015CB932700), Ph.D. Programs Foundation of Ministry of Education of China (No. 20133201110021), Natural Science Foundation of Jiangsu Province (No. BK20141200), and Priority Academic Program Development (PAPD) of Jiangsu Higher Education Institutions. The authors declare no competing financial interest.

Received: July 2, 2016
Revised: September 11, 2016
Published online:

[1] a) N. J. Jeon, J. H. Noh, W. S. Yang, Y. C. Kim, S. Ryu, J. Seo, S. I. Seok, *Nature* **2015**, *517*, 476; b) M. A. Green, K. Emery, Y. Hishikawa, W. Warta, E. D. Dunlop, *Prog. Photovoltaics* **2015**, *23*, 1.

[2] a) L. Z. Broderick, B. R. Albert, B. S. Pearson, L. C. Kimerling, J. Michel, *Sol. Energy Mater. Sol. Cells* **2015**, *136*, 48; b) F. Ghani, G. Rosengarten, M. Duke, J. K. Carson, *Sol. Energy* **2015**, *112*, 437.

[3] a) A. P. Raman, M. A. Anoma, L. Zhu, E. Rephaeli, S. H. Fan, *Nature* **2014**, *515*, 540; b) L. X. Zhu, A. Raman, K. X. Wang, M. A. Anoma, S. H. Fan, *Optica* **2014**, *1*, 32.

[4] a) X. Li, N. P. Hylton, V. Giannini, K. H. Lee, N. J. Ekins-Daukes, S. A. Maier, *Prog. Photovoltaics* **2013**, *21*, 109; b) X. Li, N. P. Hylton, V. Giannini, K. H. Lee, N. J. Ekins-Daukes, S. A. Maier, *Opt. Express* **2011**, *19*, A888; c) X. Li, Y. Zhan, C. Wang, *Prog. Photovoltaics* **2015**, *23*, 628; d) A. Shang, X. Zhai, C. Zhang, Y. Zhan, S. Wu, X. Li, *Prog. Photovoltaics* **2015**, *23*, 1734.

[5] M. G. Deceglie, V. E. Ferry, A. P. Alivisatos, H. A. Atwater, *Nano Lett.* **2012**, *12*, 2894.

[6] a) J. Nelson, *The Physics of Solar Cells*, Imperial College Press, London **2003**; b) T. J. Kucharski, Y. Tian, S. Akbulatov, R. Boulatov, *Energy Environ. Sci.* **2011**, *4*, 4449.

[7] S. Chander, A. Purohit, A. Sharma, S. P. Nehra, M. S. Dhaka, *Energy Rep.* **2015**, *1*, 175.

[8] http://www.comsol.com, FEM platform in the OET simulation. Accessed: July 2016.

[9] a) A. Shang, X. Li, *Appl. Phys. Lett.* **2015**, *106*, 051107; b) Y. Apanovich, P. Blakey, R. Cottle, E. Lyumkis, B. Polsky, A. Shur, A. Tcherniaev, *IEEE Trans. Electron. Dev.* **1995**, *42*, 890; c) T. Grasser, T. W. Tang, H. Kosina, S. Selberherr, *Proc. IEEE* **2003**, *91*, 251.

[10] A. Benvenuti, W. M. Coughran, M. R. Pinto, *IEEE Trans. Electron. Dev.* **1997**, *44*, 1349.

[11] a) V. E. Ferry, M. A. Verschuuren, H. B. T. Li, E. Verhagen, R. J. Walters, R. E. I. Schropp, H. A. Atwater, A. Polman, *Opt. Express* **2010**, *18*, A237; b) V. E. Ferry, L. A. Sweatlock, D. Pacifici, H. A. Atwater, *Nano Lett.* **2008**, *8*, 4391.

[12] a) G. K. Wachutka, *IEEE TCAD* **1990**, *9*, 1141; b) U. Lindefelt, *J. Appl. Phys.* **1994**, *75*, 942; c) J. E. Parrott, *IEEE Trans. Electron. Dev.* **1996**, *43*, 809.

[13] a) A. Deinega, S. John, *J. Appl. Phys.* **2012**, *112*, 074327; b) A. Deinega, S. John, *Comput. Phys. Commun.* **2012**, *183*, 2128.

[14] P. Wolbert, G. K. Wachutka, B. H. Krabbenborg, T. J. Mouthaan, *IEEE TCAD* **1994**, *13*, 293.

[15] a) S. Smit, W. M. M. Kessels, *J. Appl. Phys.* **2015**, *117*, 134504; b) O. Breitenstein, J. P. Rakotoniaina, *J. Appl. Phys.* **2005**, *97*, 074905.

[16] a) N. Brinkmann, G. Micard, Y. Schiele, G. Hahn, B. Terheiden, *Phys. Status Solidi RRL* **2013**, *7*, 322; b) J. Isenberg, W. Warta, *J. Appl. Phys.* **2004**, *95*, 5200.

[17] A. R. Gentle, G. B. Smith, *Sol. Energy Mater. Sol. Cells* **2016**, *150*, 39.

[18] G. Tamizh Mani, L. Ji, Y. Tang, L. Petacci, C. Osterwald, presented at *NCPV and Solar Program Review Meeting*, March **2003**, Denver, CO, USA.

[19] A. Polman, M. Knight, E. C. Garnett, B. Ehrler, W. C. Sinke, *Science* **2016**, *352*, aad4424.

© 2016 WILEY-VCH Verlag GmbH & Co. KGaA, Weinheim